Research Paper

Inlaying Radiosensitizer onto the Polypeptide Shell of Drug-Loaded Ferritin for Imaging and Combinational Chemo-Radiotherapy

Qiuhong Zhang[1,2], Jingwen Chen[3], Jie Shen[1,2], Shixiong Chen[1,2], Kaicheng Liang[1,2], Han Wang[3,4], and Hangrong Chen[1✉]

1. State Key Laboratory of High Performance Ceramics and Superfine Microstructure, Shanghai Institute of Ceramics, Chinese Academy of Sciences, Shanghai 200050, P. R. China
2. University of Chinese Academy of Sciences, 100049 Beijing, P. R. China
3. Department of Radiology, Shanghai General Hospital, Shanghai Jiao Tong University School of Medicine, Shanghai 200080, P. R. China
4. National Engineering Research Center for Nanotechnology, Shanghai 200241, P. R. China

✉ Corresponding author: hrchen@mail.sic.ac.cn

Abstract

Rationale: Ferritin with unique hollow cavity is an emerging protein-based nanoplatform for anticancer-drug delivery, but the in vivo chemotherapeutic effectiveness is still unsatisfactory with such a monotherapy modality, which is urgently in need of improvement.

Methods: Here a novel ferritin nanotheranostic with anticancer-drug doxorubicin encapsulated into its hollow interior and nanoradiosensitizer bismuth sulfide nanocrystals inlayed onto its polypeptide shell was synthesized for combinational therapeutic benefits. The formation mechanism of bismuth sulfide nanocrystals based on ferritin has been analyzed. The in vitro and in vivo treatment effects were carried out on HeLa cancer cells and tumor-bearing mice, respectively. The biocompatibility and excretion of the ferritin nanotheranostic have also been evaluated to guarantee their biosafety.

Results: The polypeptide shell of ferritin provides nucleation sites for the bismuth sulfide nanocrystals through coordination interaction, and simultaneously inhibits the further growth of bismuth sulfide nanocrystals, rendering the bismuth sulfide nanocrystals like rivets inlaying onto the polypeptide firmly, which can not only strengthen the architectural stability of ferritin to prevent drug burst leakage during systemic circulation, but also act as excellent computed tomography contrast agents and nanoradiosensitizers for in vivo imaging-guided cancer combinational treatments.

Conclusions: The design concept of inlaying bismuth sulfide nanocrystals onto the polypeptide shell of doxorubicin-encapsulated ferritin significantly inhibits the tumor growth and simultaneously further broadens the application of ferritin in nanomedicine.

Key words: ferritin, radiotherapy, chemotherapy, polypeptide subunit, bismuth sulfide

Introduction

Cancer remains one of the deadliest diseases and causes millions of deaths every year. Currently, the anticancer drugs such as doxorubicin (Dox) that can induce cytotoxic activity by oxidative DNA damage and subsequent inhibition of topoisomerase II to block DNA replication inside the nucleus [1], have been well-received for cancer chemotherapy [2-6]. However, when administrated directly in vivo, Dox and other small-molecular drugs share similar disadvantages of short blood circulation time,

life-threating cardiotoxicity, and multi-drug resistance after repeated administrations. To circumvent these limitations, researches on drug delivery systems have garnered burgeoning attention and advanced rapidly in nanomedicine. To date, there are a myriad of nanomaterials have been designed and synthesized to serve as drug delivery systems for combating cancer, among which, biologically compatible proteins are highly favorable for drug loading and in vivo drug delivery [4, 7-9], owing to their prominent merits of inherent biological origin, excellent biocompatibility and low immunogenicity.

Ferritin is a natural iron-storage protein assembled by the interaction of 24 polypeptide subunits which creates a spherical conformation with an external diameter of ~12 nm and an internal cavity of ~8 nm. The ferritin can be reversibly disassembled when the pH milieu becomes extremely acidic or basic, and the disassembled polypeptide subunits are able to self-assemble into intact ferritin again when the pH milieu returns to neutrality. Such an interesting pH triggered assembly and disassembly behavior makes it a good candidate as drug delivery system to encapsulate chemotherapeutic drugs into its hollow cavity for cancer chemotherapy. For example, the Dox molecules, as a kind of model drug, are reported to be encapsulated into ferritin for anticancer. Though much effort has been made to improve the Dox loading amount, including the fabrication of channel opened ferritin to facilitate drug loading [4, 10, 11], the in vivo therapeutic effectiveness is still unsatisfactory with such a monotherapy modality. Therefore, additional therapeutics is expected to combine with drug-loaded ferritin for high-efficient tumor regression.

Radiotherapy (RT), which utilizes ionizing radiation (X-ray) to cause DNA damage to ablate tumor without depth restriction [12, 13], is clinically employed to cooperate with chemotherapy. Recently, inorganic nanomaterials containing high Z elements (such as elements of Au [14-16], W [17], Bi [18-24], etc.) have been widely investigated as nanoradiosensitizers. Compared with pure RT, during which high-energy X-rays are applied to tumorous regions to kill cancer cells, those nanoradiosensitizers that accumulate in tumorous regions through the enhanced permeability and retention (EPR) effect [25-27] can interact with X-rays, producing photoelectrons, compton electrons, and secondary charged particles to promote RT-induced cancer killing [15]. Therefore, nanoradiosensitizers-enhanced RT combines with drug-loaded ferritin hold out great promise for eventual effective tumor ablation, which, however, poses challenges for the material design based on ferritin.

Ferritin has attracted wide attention for its hollow cavity, with attention rarely being devoted to its polypeptide shell. Practically, the polypeptide shell of ferritin could also be used to synthesize nanotherapeutics, because growing evidences suggest that the functional groups (e.g., -SH, -NH$_2$, -COOH) in the polypeptide can bind various metal ions, such as Cu^{2+}, Ag$^+$, Cd^{2+}, etc. [18, 22, 28-32]. Thus, integrating nanoradiosensitizers on the shell of drug-loaded ferritin is feasible for combinational therapeutic benefits.

Herein, for the first time, a novel kind of ferritin nanotheranostic, with anticancer drug Dox encapsulated into its hollow interior and nanoradiosensitizer bismuth sulfide nanocrystals growing onto its polypeptide shell, was synthesized for computed tomography (CT) imaging-guided cancer combinational chemo-radiotherapy. The design concept of inlaying bismuth sulfide nanocrystals on the polypeptide shell of ferritin has the benefits as follows: strengthen the architectural stability of ferritin to prevent drug burst leakage during systemic circulation; act as contrast agents for CT imaging owing to large X-ray attenuation coefficient of bismuth element; promote the RT induced cancer cell-killing based on the radio-sensitization effect. More importantly, thanks to the Dox benefited chemotherapy of ferritin nanotheranostic, accompanying with bismuth sulfide nanoradiosensitizer-enhanced RT efficacy, the tumor growth was significantly inhibited and the survival rate of tumor-bearing mice was remarkably improved.

Results and Discussion

Synthesis and characterizations of Dox@AFBS

The encapsulation of anticancer drug Dox into ferritin was according to the previous method with modifications [10]. Briefly, as illustrated in Figure 1A, apoferritin (AFn, iron-devoid spherical protein shell of ferritin) was dispersed in the Dox glycine-acetate buffer (pH < 4) to disassemble the polypeptide subunits, then the solution was slowly adjusted to pH ~ 7.4 to reassemble AFn and dialyzed to remove free Dox molecules. Next, the Dox-loaded AFn (denote as Dox@AFn) was incubated with mannitol stablized bismuth nitrate to form Dox@AFn-Bi^{3+} complexes, followed by the addition of thioacetamide to provide sulfur source. After further reaction for 3 h at room temperature, the bismuth sulfide nanocrystals were synthesized on the protein shell of Dox@AFn (denote as Dox@AFBS). The photographs of AFn, Dox@AFn and Dox@AFBS solutions are displayed in Figure 1B, owing to the synthesis of bismuth sulfide nanocrystals

onto the protein shell, the color of the obtained Dox@AFBS solution was quite different from the Dox@AFn and AFn solutions. However, the hydrodynamic size of Dox@AFBS is almost identical to that of the Dox@AFn and AFn solutions (Figure S1). Figure 1C presents the X-ray diffraction pattern of the Dox@AFBS, whose diffraction peaks can be well indexed to the orthorhombic Bi_2S_3 (JCPDS Card No.17-0320). The transmission electron microscopy (TEM) image at low magnification demonstrates that the obtained Dox@AFBS has a uniform size (Figure 1D), which is consistent with its hydrodynamic size result (Figure S1). The TEM image of an individual Dox@AFBS (Figure 1E) reveals that the Bi_2S_3 nanocrystals indeed grow on the shell of AFn. Figure 1F shows the high resolution TEM image of selected area in Figure 1E, which further evidences the ultra-small Bi_2S_3 nanocrystals have been inlayed in the polypeptide subunits, and the d-spacing of lattice fringes was determined to be 0.357 nm, well in consistence with (130) lattice plane of orthorhombic Bi_2S_3 phase. The chemical composition of Dox@AFBS was confirmed by energy-dispersive X-ray analysis, as shown in Figure 1G, the C, N and O elements

mainly derived from AFn and Dox molecules, and Bi and S elements with atom ratio of about 2:3 (Table S1) stem from Bi_2S_3 nanocrystals. Together, these results manifest the successful synthesis of Bi_2S_3 nanoradiosensitizers onto the polypeptide shell of AFn.

Formation mechanism of Bi_2S_3 nanocrystals based on AFn

The polypeptide of AFn was scarcely reported for the synthesis of inorganic nanoparticles, and this is the first endeavor to synthesize ultra-small Bi_2S_3 nanoradiosensitizers onto the polypeptide shell, thus figuring out the formation mechanism of Bi_2S_3 nanocrystals is of great significance. To directly investigate the formation mechanism of Bi_2S_3 nanocrystals based on AFn, drug unloaded AFn was incubated with mannitol stablized bismuth nitrate to form AFn-Bi^{3+} complexes, followed by the addition of thioacetamide and further reaction for 3 h at room temperature. The Bi_2S_3 nanocrystals synthesized with AFn (denote as AFBS) shows the microstructure similar to that of Dox@AFBS (Figure S2). To further study the interaction between AFn and Bi_2S_3
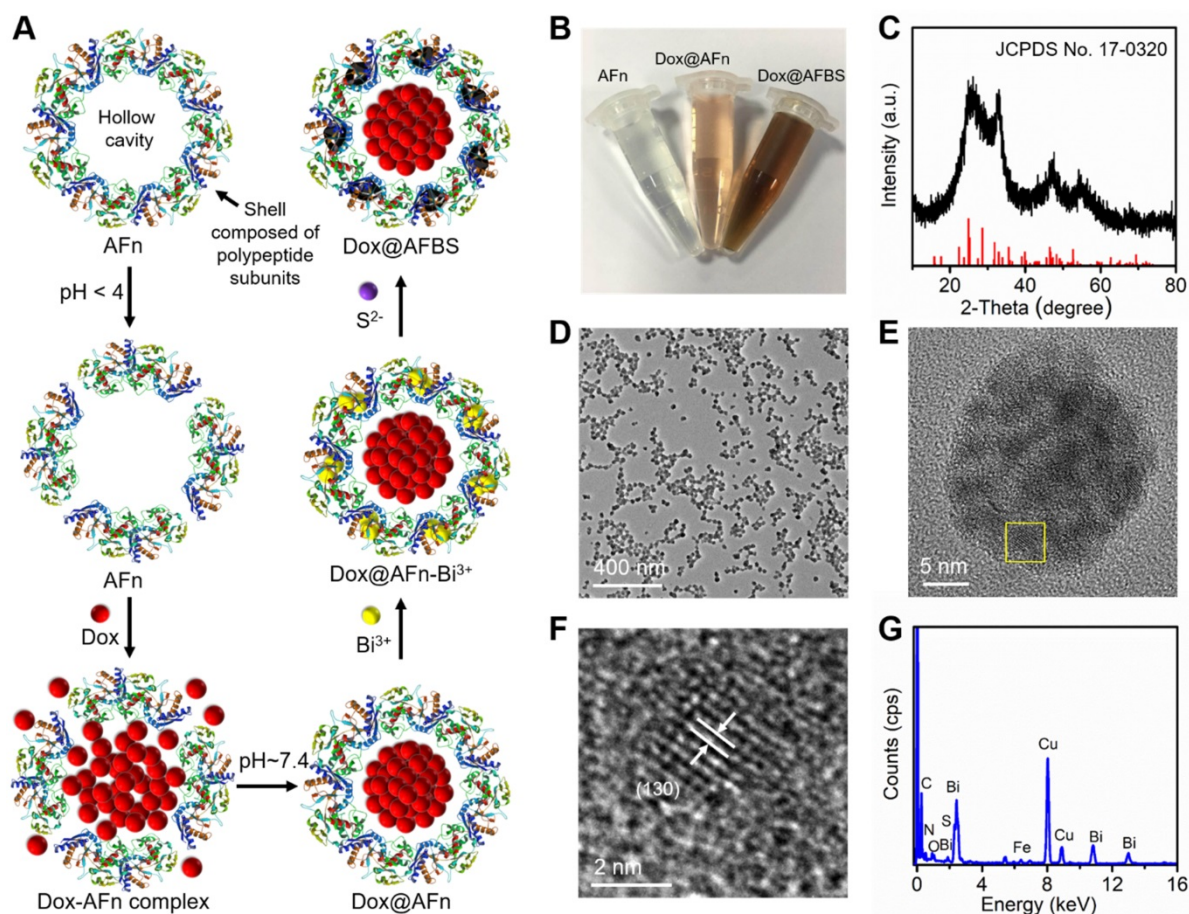

Figure 1. (A) Synthetic procedures of Dox@AFBS. (B) Photograph of obtained AFn, Dox@AFn and Dox@AFBS aqueous solutions. (C) X-ray diffraction pattern of the Dox@AFBS. TEM images of Dox@AFBS at (D) low and (E, F) high magnifications. (G) Corresponding energy-dispersive X-ray analysis.

nanocrystals detailedly, the fourier transform infrared spectroscopy (FTIR) of AFn, AFn-Bi^{3+}, AFBS after reaction for 1 h (denote as AFBS-1 h), 2 h (denote as AFBS-2 h) and 3 h (denote as AFBS-3 h), respectively, were recorded and analyzed. As presented in Figure 2A, the peak at 663 cm^{-1} originates from the bending vibration of NH$_2$, after adding bismuth source to AFn solution, the peak at 519 cm^{-1} corresponds to the bismuth vibration was observed [33], and meanwhile, the peak at 1388 cm^{-1} that mainly belongs to the bending vibrations of -OH and N-H groups [33], shifted to 1396 cm^{-1}. These results indicate that there could be coordination interaction between Bi^{3+} ions and N-H groups of AFn, which was considered to be very beneficial for the nucleation of Bi$_2$S$_3$ nanocrystals onto the polypeptide shell of AFn. Furthermore, it is found that the aforementioned peaks show no obvious changes in the FTIR spectra of AFBS and AFn-Bi^{3+}, suggesting that the coordination interaction between Bi^{3+} ions and N-H groups existed in the whole reaction process, which could be responsible for the stable nucleation and growth of Bi$_2$S$_3$ nanocrystals on the polypeptide shell of AFn.

Next, the circular dichroism (CD) spectroscopy which can reflect the conformational changes of the secondary structures of AFn in the reaction system, was utilized to further clarify the formation mechanism of the Bi$_2$S$_3$ nanocrystals based on AFn. As shown in Figure 2B, the CD spectrum of AFn displays a positive peak at 190 nm and two negative peaks at 209 nm and 222 nm, respectively. However, comparing the CD spectrum of AFn with that of AFn-Bi^{3+}, the peak at 209 nm was observed to shift to a low wavelength and the intensities of all the peaks declined. Moreover, the addition of sulfur source and subsequent reaction for 3 hours further weakened the intensities of all the peaks. Based on the CD spectra, the conformational changes of AFn were calculated and summarized in Table 1, which clearly reveals the continuous content decrease of α-Helix, the main secondary structure of ferritin. Particularly, much changes of α-Helix were observed for AFn-Bi^{3+} and AFBS-1 h. On average, there are 3.6 amino acid residues in every ring of α-Helix, thus the coordination interaction between Bi^{3+} ions and N-H groups might mainly locate in the α-Helix, which effectively accounts for the initial conformational changes of AFn-Bi^{3+}. Furthermore, in combination with previous report that the hydrogen bond formed between the oxygen atom of the C=O group and the hydrogen atom of the N-H group is a key factor to stable the α-Helix structure [34], it can be inferred that the nucleation and growth of Bi$_2$S$_3$ nanocrystals benefited from the coordination interaction might have broken such hydrogen bond, resulting in the content decrease of α-Helix for AFBS-1 h, AFBS-2 h and AFBS-3 h, which thereafter transforms into other secondary structures, such as β-Sheet, Turn and Random coil. Additionally, the CD spectrum of AFBS-2 h is almost identical to that of AFBS-3 h, manifesting the further growth of Bi$_2$S$_3$ nanocrystals was prevented as a consequence of the space limitation of the secondary structures of the polypeptide. Therefore, the polypeptide of AFn not only provides nucleation sites for the Bi$_2$S$_3$ nanocrystals through coordination interaction, but also inhibits the further growth of Bi$_2$S$_3$ nanocrystals, rendering the Bi$_2$S$_3$ nanocrystals like rivets inlayed onto the polypeptide shell of AFn firmly.

Table 1. Conformational changes of the secondary structures of AFn, AFn-Bi^{3+} and AFBS (-1 h, -2 h, -3 h).

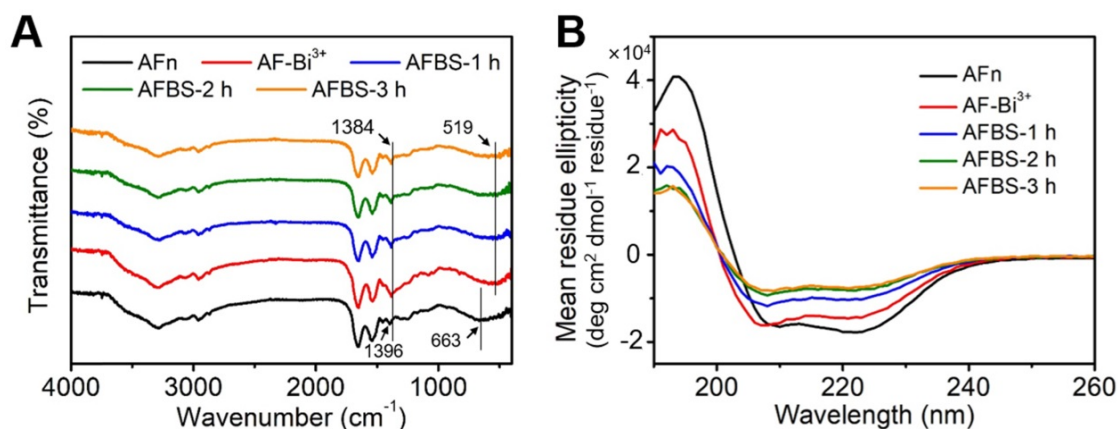|	α-Helix	β-Sheet	Turn	Random coil
AFn	0.598	0.073	0.134	0.182
AFn-Bi^{3+}	0.438	0.144	0.177	0.256
AFBS-1 h	0.325	0.168	0.211	0.306
AFBS-2 h	0.277	0.196	0.220	0.287
AFBS-3 h	0.254	0.219	0.220	0.282

Figure 2. (A) The FTIR spectra of AFn, AFn-Bi^{3+} and AFBS (-1 h, -2 h, -3 h). (B) The CD spectra of AFn, AFn-Bi^{3+} and AFBS (-1 h, -2 h, -3 h).
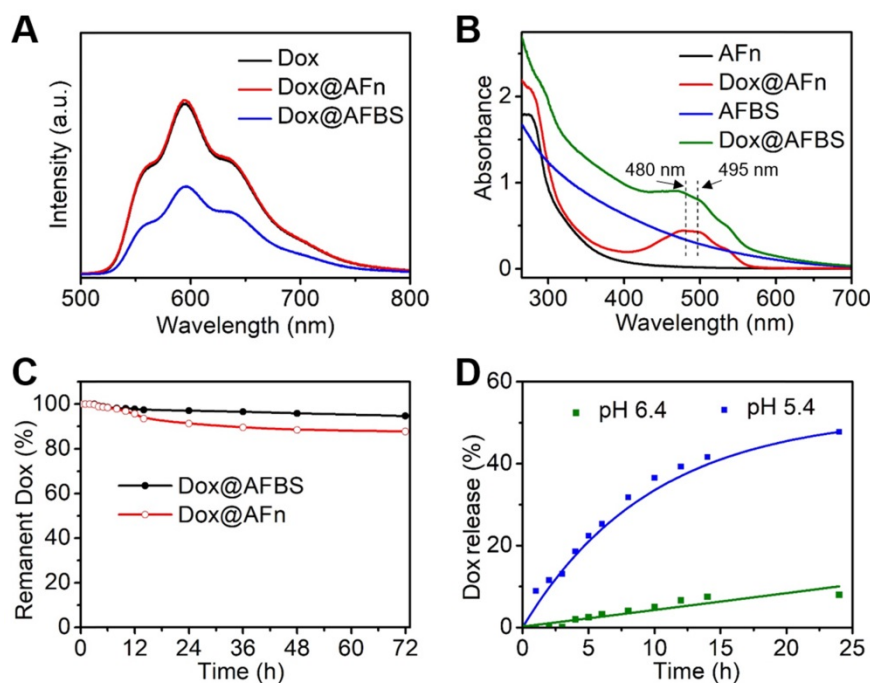
Figure 3. (A) Fluorescence spectra of Dox, Dox@AFn and Dox@AFBS solutions excited at 470 nm. (B) UV-Vis absorption spectra of AFn, Dox@AFn, AFBS and Dox@AFBS solutions. (C) Drug stability analysis of Dox@AFBS and Dox@AFn incubated in buffer with a pH value of 7.4 at 37 °C for 3 days. (D) Dox release from Dox@AFBS at pH 5.4 and pH 6.4 at 37 °C.

Evaluations of drug loading and drug release of Dox@AFBS

Next, the drug loading of Dox@AFBS was investigated. As shown in Figure 3A, the Dox@AFn shows strong red fluorescence comparable to that of Dox molecules, which, however, attenuates after the inlay of Bi_2S_3 nanocrystals onto the polypeptide shell. This is because the fluorescence emission of Dox molecules encapsulated in the hollow cavity of AFn has been partially absorbed by the Bi_2S_3 nanocrystals on the shell. In addition, the UV-Vis spectroscopy was also employed to evaluate the drug loading. As shown in the Figure 3B, the UV-Vis absorption spectrum of Dox@AFn retains the characteristic absorption peaks (480, 495 nm) of Dox molecules, and the zeta potential of Dox@AFn is similar to that of AFn (Figure S3), demonstrating the Dox molecules were successful encapsulated into the interior of AFn rather than the outer surface. Moreover, such characteristic absorption of Dox also presents in the UV-Vis absorption spectrum of Dox@AFBS, which simultaneously exhibits a broad absorption similar to that of AFBS, further evidencing the AFn can not only carry Dox molecules into its hollow cavity, but also facilitate the synthesis of Bi_2S_3 nanocrystals on the polypeptide. The Dox concentration was determined by measuring the UV-Vis absorbance at 480 nm and thereafter calculating based on the calibration curve of Dox (Figure S4), the concentrations of bismuth element and AFn were determined using inductively coupled plasma optical emission spectrometry (ICP-OES) and bicinchoninic acid protein assay, respectively. According to the calibration curve of Dox, ICP-OES and bicinchoninic acid protein analysis, it is estimated that the mass ratio of Dox to bismuth to AFn was 0.026: 0.21: 1 for the obtained Dox@AFBS.

The drug stability of Dox@AFBS was evaluated by incubating Dox@AFBS in the normal physiological environment with a pH value of 7.4 at 37 °C, followed by the monitoring of Dox release. As shown in the Figure 3C, drug leakage was scarcely detected over 6 h period of incubation and no more than 10% drug leakage from Dox@AFBS was detected post incubation for 3 days, which is highly favorable for systemic circulation without concerning about drug burst leakage. For comparison, we also evaluated the drug stability of Dox@AFn and found that nearly 15% drug was leaked from Dox@AFn during 3 days, which is higher than that of Dox@AFBS. We speculate that the Bi_2S_3 nanocrystals inlayed onto the polypeptide shell of AFn might have strengthened the architectural stability of Dox@AFBS.

Since AFn can disassemble into polypeptide subunits under acidic condition and release its payloads, the drug-releasing of Dox@AFBS is evaluated by incubating Dox@AFBS in different pHs of 5.4 and 6.4, which can simulate the lysosome environment of tumor cell and tumor microenvironment, respectively. As shown in the Figure 3D, no significant Dox release was observed when bathed in a pH 6.4 milieu for 5 h, and the

amount of released Dox was no more than 10% after 24 h. In contrast, sustained Dox release was observed when bathed in a pH 5.4 milieu for 24 h and the release amount was up to 50%, which could attribute to the expansion of protein cage triggered by the more acidic condition. These results suggest that the Dox@AFBS favors potential Dox release in acidic lysosome compartment of cancer cells.

In vitro cellular drug release and therapeutic benefit of Dox@AFBS

Before the investigation of cell uptake, we evaluate the dispersion stability of Dox@AFBS in phosphate-buffered saline (PBS), fetal bovine serum (FBS) and Dulbecco's modified Eagle medium (DMEM). As shown in Figure S5, the Dox@AFBS can stably dispersed in these media without precipitation, indicating that the Dox@AFBS possesses excellent stability. Then Dox@AFBS with a Dox concentration of 10 µg mL^{-1} was used to co-incubate with human cervical carcinoma (HeLa) cells for 1 h, 2 h and 4 h, followed by the detection of Dox fluorescence in HeLa cells with flow cytometry. As shown in Figure 4A, the intracellular Dox fluorescence gradually increases when prolongs the incubation time from 1 h to 4 h, indicating the Dox@AFBS has been endocytosed into HeLa cells.

To further study the Dox release in cancer cells triggered by the endogenic acidic stimulus, LysoTracker Green labeled lysosome and 4',6-diamidino-2-phenylindole (DAPI) stained nucleus of HeLa cells incubated with Dox@AFBS over time were monitored using confocal laser scanning microscopy. As shown in Figure 4B, bright yellow fluorescence as a result of the co-localization between Dox@AFBS and lysosomes can be clearly observed after incubation for 4 h, evidencing that the Dox@AFBS was located in lysosomes. Moreover, a small amount of red Dox fluorescence can also be visualized in the nucleus, indicating a part of Dox molecules have been released from Dox@AFBS triggered by the acidic milieu in lysosomes and thereafter delivered into cell nucleus. After prolonging the incubation time to 12 h, we found that yellow fluorescence declined, whereas bright red Dox fluorescence throughout the cell nucleus (Figure 4C), manifesting that most of Dox@AFBS were escaped from the lysosomes, and substantial Dox molecules were released and delivered into cell nucleus, which was highly beneficial for cancer cell-killing.

The in vitro treatment effect of Dox@AFBS was examined by a standard cell counting kit-8 (CCK-8) assay. The cytotoxicity of AFBS at various bismuth concentrations was tested through incubating with HeLa cancer cell and HUVE (human umbilical vein endothelial) normal cell for 24 h. The results show that the AFBS has little effects on cell viability, even at a high bismuth concentration up to 200 µg mL^{-1} (Figure 5A). For in vitro RT analysis, HeLa cells incubated with AFBS at various bismuth concentrations were radiated under clinical 220 keV X-rays at a dose of 8 Gy (denote as AFBS+RT). As shown in Figure 5B, cells treated with AFBS+RT exhibit lower cell viability compared with pure RT, and cell viability is significantly decreased with AFBS+RT if the bismuth concentration is higher than 100 µg mL^{-1}, indicating the efficient radio-sensitization effect of AFBS. The cytotoxicities of Dox@AFBS, Dox@AFn and Dox were also parallelly evaluated. The results reveal that both Dox@AFBS and Dox@AFn were as toxic as free Dox against HeLa cells at a high Dox concentration. However, Dox@AFBS and Dox@AFn show a little more toxic than free Dox to cancer cells at a low Dox concentration of <6.25 µg mL^{-1}, which might attribute to the faster endocytosis of Dox enabled by AFn nanocarrier (Figure 5C). For combinational treatment analysis, cells incubated with Dox@AFBS were subjected to RT treatment. As indicated in Figure 5D, much enhanced inhibition of cell proliferation was achieved owing to the extra radio-sensitization effect of Bi_2S_3 nanoradiosensitizers.

In vivo imaging-guided combinational treatment

Prior to in vivo tumor treatment, the tumor accumulation of Dox@AFBS was investigated by imaging, since the large X-ray attenuation coefficient of bismuth element enables Dox@AFBS as contrast agent for CT imaging. As shown in Figure 6A, the CT imaging performance can be directly visualized through a set of CT images of Dox@AFBS solutions with different bismuth concentrations. Hounsfield unit (HU) value and Dox@AFBS concentration present an linearity with a slope up to ~126.8 HU L·g^{-1} (Figure 6B), which is much higher than that of the clinically used CT contrast agent iopromide (15.9 HU L g^{-1}) [22]. Encouraged by the in vitro strong CT contrast peformance, Dox@AFBS with a bismuth dose of 30 mg kg^{-1} and Dox dose of 3.75 mg kg^{-1}, was further intravenously (i.v.) injected into HeLa tumor-bearing mice, and in vivo CT images were acquired pre-injection and at 24 h post-injection. As shown in Figure 6C, the CT contrast of tumor increases from 21.25 HU to 46.42 HU, indicating the effective tumor accumulation of Dox@AFBS through the EPR effect. The tumor accumulation of Dox@AFBS was also verified by ICP-OES quantitative analysis. The results reaveal that Dox@AFBS shows longstanding retention in tumor and reaches a maximal tumor accumulation at 24 h post-injection,

with a tumor uptake value of 0.585% injected dose (Figure S6), which is comparable to the reported tumor uptake level of ~0.6% for a majority of nanomaterials [35].
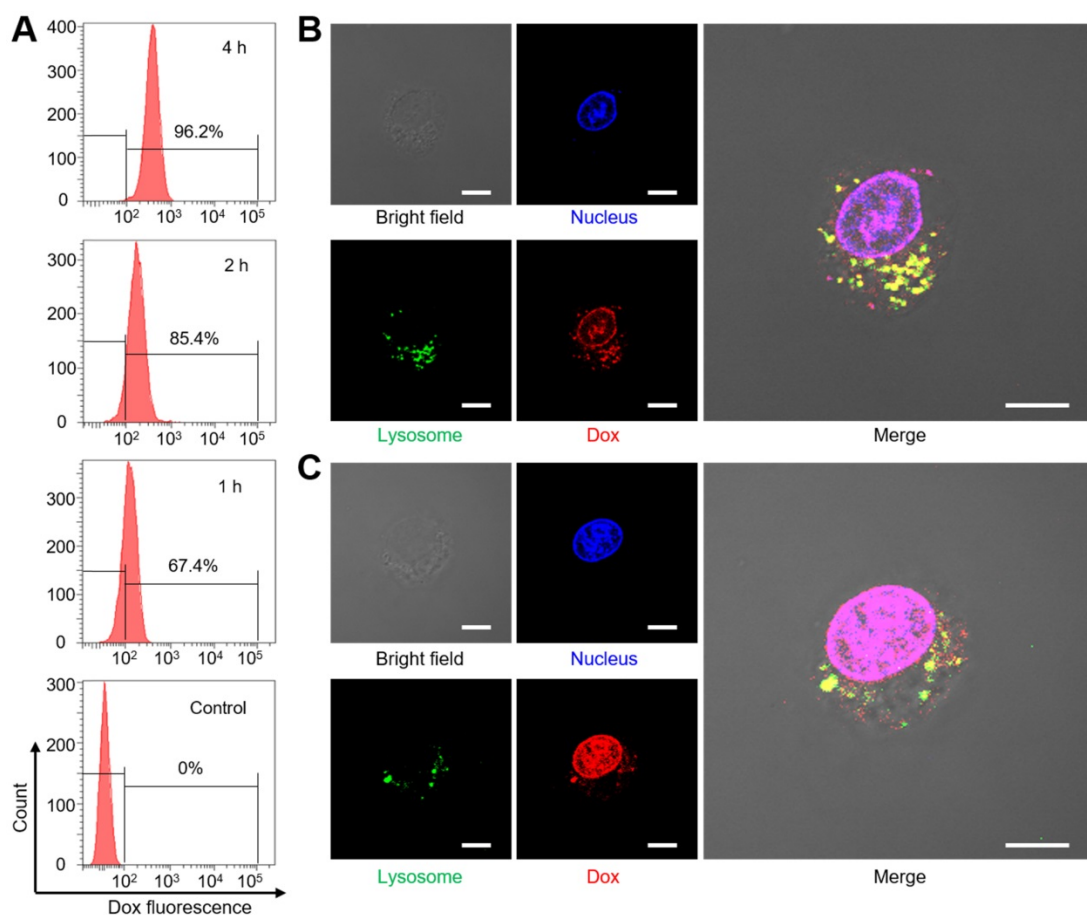

Figure 4. (A) Uptake analysis of Dox@AFBS in HeLa cells with flow cytometry. Confocal fluorescence images of cells after incubation with Dox@AFBS for (B) 4 h and (C)12 h. The nucleus and lysosomes were stained by LysoTracker Green and DAPI, respectively. Yellow fluorescence refers to the merge of red and green fluorescence. The bright field shows the morphology of HeLa cells. Scale bars are 10 μm.
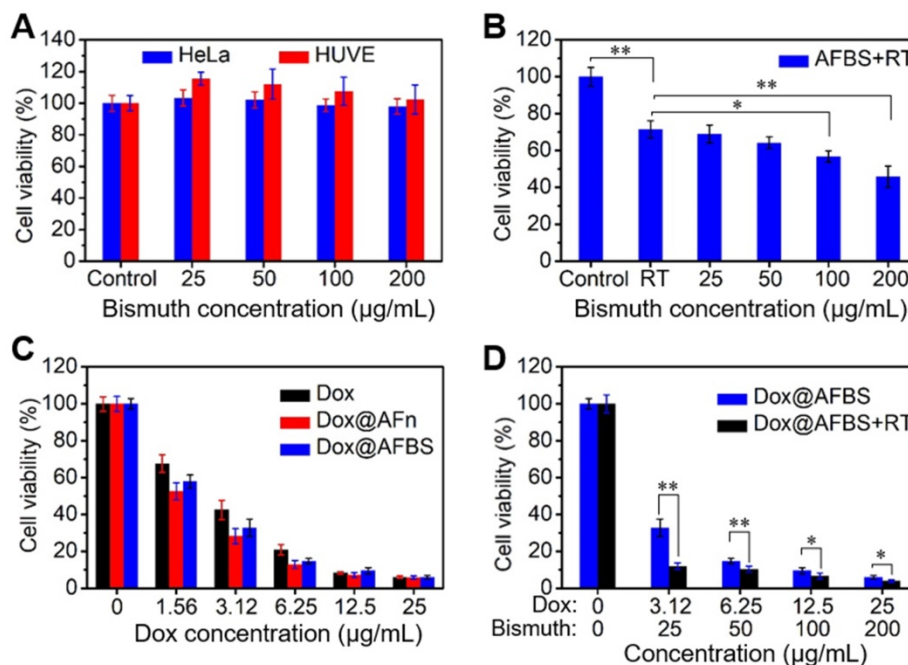

Figure 5. (A) Relative cell viability of HeLa and HUVE cells treated with AFBS at various bismuth concentrations. (B) Relative cell viability of HeLa cells treated with AFBS at various bismuth concentrations under radiation dose of 8 Gy. (C) Relative cell viability of HeLa cells treated with Dox, Dox@AFn and Dox@AFBS at various Dox concentrations. (D) Relative cell viability of HeLa cells treated with Dox@AFBS under radiation dose of 8 Gy.
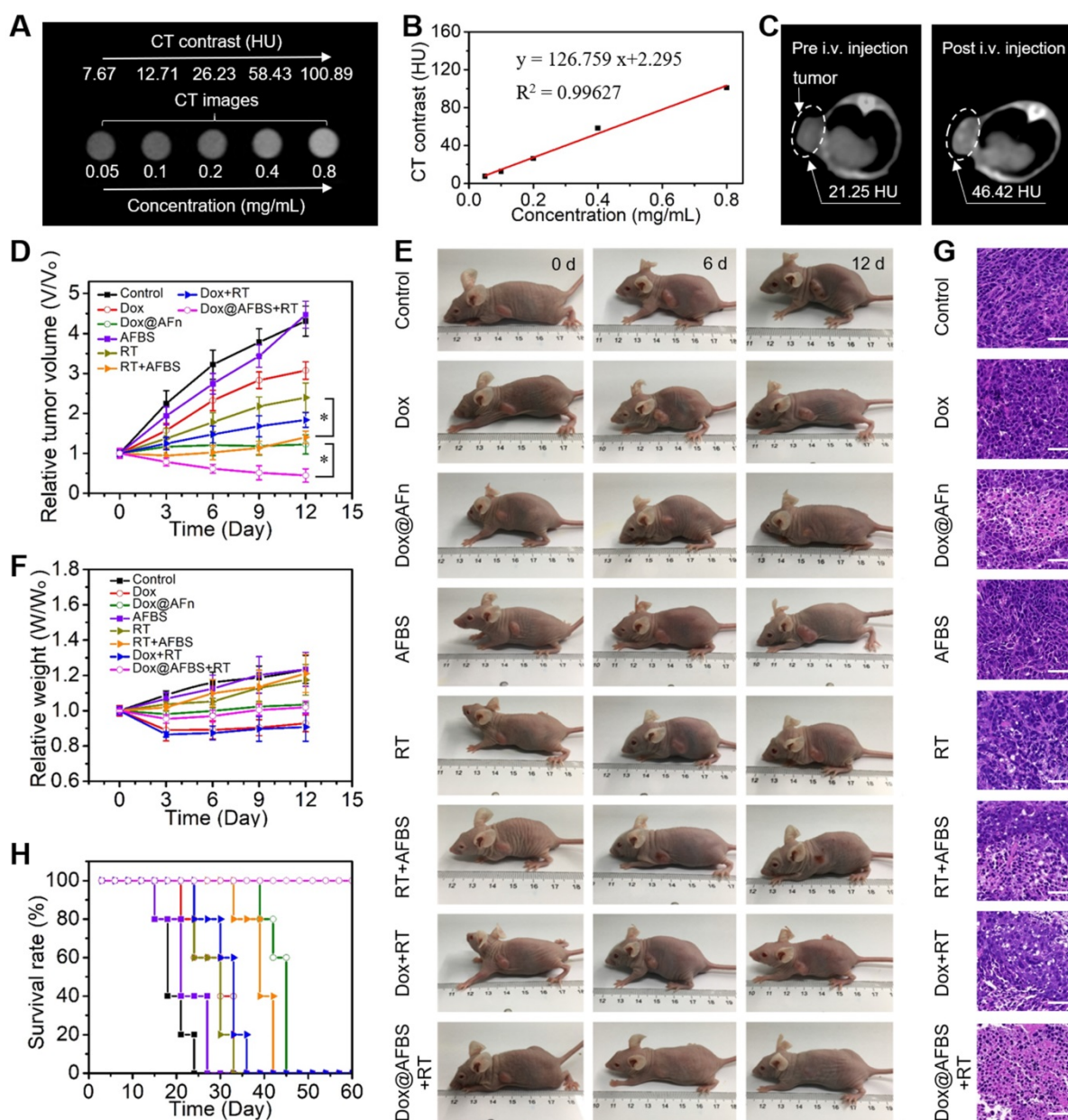
Figure 6. (A) In vitro CT images of Dox@AFBS solutions with different bismuth concentrations. (B) CT contrast of Dox@AFBS as a function of bismuth concentration. (C) In vivo CT images of HeLa tumor-bearing mice pre and post i.v. injection of Dox@AFBS. (D) Tumor growth curves of mice after various treatments for 12 days (n = 5, mean ± standard deviation, *P < 0.05, one-way analysis of variance). (E) Digital photos of tumor-bearing mice in different groups taken on the 0, 6 and 12th day after treatment. (F) Corresponding body weights of mice after various treatments for 12 days. (G) Micrographs of H&E-stained tumor slices collected from different groups of mice on the third day after treatment. Scale bars are 50 μm. (H) The survival rate of mice after various treatments.

Motivated by the excellent in vitro combinational chemo-radiotherapy effect and the effective tumor accumulation, in vivo tumor treatment was further conducted. The HeLa tumor bearing mice were randomly divided into eight groups, i.e., control, Dox, Dox@AFn, AFBS, RT, AFBS+RT, Dox+RT, and Dox@AFBS+RT groups, respectively. The clinical 220 keV X-ray at a dose of 8 Gy was used for RT treatment and the X-ray radiation area was fixed at 10 mm×10 mm which is enough to cover the tumor of a mouse. The mice in all groups received one injection, and the injected dose of bismuth and Dox is 30 mg kg⁻¹ and 3.75 mg kg⁻¹,

respectively. The RT treatment was conducted at 24 h post-injection due to the above disscused maximal tumor accumulation of Dox@AFBS at this time point. After various treatments, the tumor volume and body weight of mice were recorded every 3 days. As shown in Figure 6D, the AFBS group presents a tumor growth curve similarly to that of the control group, indicating AFBS has no therapeutic effect on the tumor. Compared with the RT group that the X-ray irradiation was only able to partially inhibit the tumor growth, the AFBS+RT group shows significant tumor growth inhibition, due to the radiosensitizing effect of Bi_2S_3 nanoradiosensitizers on the polypeptide shell of

AFn. Moreover, because of the effective intratumor delivery of Dox molecules by AFn nanocarrier through EPR effect, the tumor growth in Dox@AFn group compared with direct Dox administration group, was obviously inhibited. Most remarkbly, it is found that the Dox@AFBS+RT group exhibits the most effective tumor growth inhibition effect, which is mainly attributed to the combinational effect of intratumor Dox delivery with AFn and radio-sensitization with Bi_2S_3 nanocrystals inlayed on AFn. The corresponding photos of mice after various treatments are shown in Figure 6E, it is evident that the Dox@AFBS+RT treated mice show the smallest tumor size. Meanwhile, the weights of mice in Dox@AFBS+RT group are stably increasing during the treatment period, indicating the negligible adverse effects of such combinational treatment protocol on the mice (Figure 6F). To further evaluate the therapy efficacy, 3 days after various treatments had been administered, tumors from different groups were dissected for hematoxylin and eosin (H&E) staining. As shown in Figure 6G, the condensation of nuclear chromatin and cytoplasmic shrinkage are the typical characteristics of cell apoptosis, clearly demonstrating the Dox@AFBS+RT therapeutic protocol causes the most severe damage to tumor by inducing tumor cell apoptosis. The remarkably improved survival rate of Dox@AFBS+RT treated mice further confirms such highly efficient therapeutic effect (Figure 6H).

Biosafety of combinational treatment

Furthermore, the biosafety of Dox@AFBS+RT combinational therapeutic protocol was assessed. The Dox@AFn has been previously evaluated of excellent biosafety that significantly reduced healthy organ drug exposure [4], thus we examined the biodistribution of bismuth element in main tissues of mice. The tumor-bearing mice after receiving administration of Dox@AFBS were sacrificed at the indicated time points, and then the bismuth contents in the main organs were analyzed using ICP-OES. As shown in Figure 7A, the Dox@AFBS mainly accumulates in reticuloendothelial systems such as liver and spleen after administration for 1 day, a typical phenomenon for the nanomaterials after systemic administration. But it was quickly eliminated from liver and spleen on the 2nd day, with continuous elimination in the following days. Despite Dox@AFBS shows accumulation in lung at 4 h post administration, rapid elimination was observed on the 1st day. Because of the urine pathway for in vivo clearance, a small quantity of bismuth element was detected in the kidney during the whole treatment period of 12 days. Therefore, we speculate that the Dox@AFBS was mainly excreted from body through feces. It is noteworthy that bismuth element was scarcely detected in the heart, suggesting the low accumulation of Dox@AFBS within heart, thus the chemotherapy with risk of cardiotoxicity can be effectively circumvented. It is calculated that less than 15% injected dose of bismuth per gram of tissues (ID g^{-1}) can be detected from the normal tissues of mice after administration for 12 days, indicating the effective excretion of Dox@AFBS, which largely relieves the mice from potential long-term toxicity caused by nanomaterials without biodegradation and clearance in vivo. Moreover, H&E-stained major tissues from mice in Dox@AFBS+RT group were also analyzed on the 12th day, which shows no histological lesions in comparison with control group (Figure 7B). Together, these results effectively manifest that the Dox@AFBS+RT therapeutic protocol is of high biosafety.

Conclusions

A novel kind of ferritin nanotheranostic (i.e., Dox@AFBS), with anticancer-drug Dox encapsulated into its hollow interior and Bi_2S_3 nanocrystals inlayed onto its polypeptide shell, was firstly constructed for CT imaging-guided
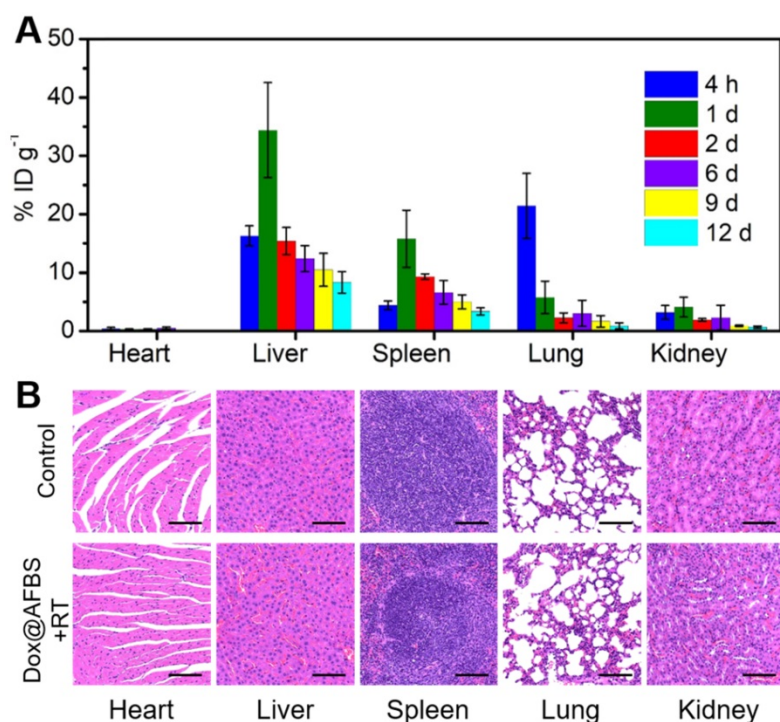

Figure 7. (A) Time-dependent biodistribution of bismuth element [% injected dose (ID) of bismuth per gram of tissues] in main tissues of mice after i.v. injection of Dox@AFBS. (B) Micrographs of H&E-stained major tissues from mice in control and Dox@AFBS+RT groups after treatments for 12 days. Scale bars are 100 μm.

cancer combinational treatment. The coordination interaction between Bi^{3+} ions with N-H groups facilitates the nucleation of Bi_2S_3 nanocrystals on the secondary structures of the polypeptide. Because of the space limitation of the secondary structures of the polypeptide, the further growth of Bi_2S_3 nanocrystals was prevented, rendering the Bi_2S_3 nanocrystals like rivets firmly inlaying onto the polypeptide shell of ferritin. The Bi_2S_3 nanocrystals onto the polypeptide shell can strengthen the architectural stability of Dox@AFBS to prevent drug burst leakage, while the encapsulated Dox molecules can selectively release in the mildly acidic lysosome compartment and induce cancer cells death consequently. Moreover, the Bi_2S_3 nanocrystals onto the polypeptide shell can act as contrast agents for CT imaging, which can indicate the efficient tumor accumulation of Dox@AFBS through EPR effect after systemic administration, offering imaging guidance for in vivo cancer treatment. More importantly, the enhancement of RT efficacy based on Bi_2S_3 nanoradiosensitizer, together with the combinational effect of chemotherapy, significantly inhibit the tumor growth and remarkably improve the survival rate of tumor-bearing mice. In addition, such combinational treatment protocol was evaluated of high biosafety, inducing no harms on the mice. It is worth noting that our design concept of inlaying ultra-small nanocrystals onto the polypeptide shell of ferritin not only further broadens its application in nanomedicine, but also provides a new idea for the construction of multifunctional core-shell nanostructures based on ferritin, which may show unique advantages in other research fields.

Materials and Methods

Materials

The Dox was obtained from Sangon Biotech. Horse spleen apoferritin was obtained from Sigma-Aldrich. Bismuth nitrate and mannitol were obtained from Aladdin Industrial Co. Thioacetamide was obtained from J&K Chemical Co. Hydrochloric acid, glycine, and sodium hydroxide was obtained from Sinopharm Chemical Reagent Co. All chemicals were used as received without further purification.

Preparation of Dox@AFBS

The Dox loading was prepared as described by Kilic et al.[10] with modifications. Briefly, apoferritin (10 mg) was dispersed in Dox (1 mg/mL) glycine-hydrochloric acid buffer (pH < 4) to disassemble the polypeptide subunits. The pH of the mixture was slowly adjusted to 7.4 with sodium hydroxide (1 M) to resemble the polypeptide subunits. The resulting solution was dialyzed for 24 h to remove free Dox molecules. Then, the Dox-loaded apoferritin (10 mg of apoferritin) was incubated with mannitol stablized bismuth nitrate (200 mM, 200 µL), followed by the addition of thioacetamide (300 mM, 200 µL) and further reaction for 3 h at room temperature.

Characterization of Dox@AFBS

TEM images and Energy-dispersive X-ray analysis were obtained with JEM-2100F. X-ray diffraction measurement was conducted on a Rigaku D/MAX-2250 V instrument (Cu Kα radiation, λ = 0.154056 nm, scanning rate of 4° min^{-1}). Fluorescence spectra and UV-Vis spectra were recorded on a SHIMADZU RF-6000 spectrophotometer and SHIMADZU UV-2600 spectrophotometer, respectively. Elemental quantitative analysis was determined using ICP-OES. Protein quantification was determined using bicinchoninic acid protein assay. The secondary structure of protein was analyzed using chirascan CD spectrometer.

Dox releasing of Dox@AFBS

The Dox@AFBS dispersed in dialysis bag (MW 3600) was incubated with 20 mL of PBS (pH 6.4 or 5.4) at 37 °C. At indicated time points, withdraw 1 mL of release medium and replenish an equal volume of blank medium. The release medium was diluted and assayed by UV-Vis spectra. The released Dox at different incubation times was calculated by the calibration curve of Dox.

Cellular culture

HeLa and HUVE cells were cultured in DMEM containing 10 % FBS and 1 % penicillin/streptomycin at 37 °C in humidified atmosphere with 5% CO_2.

Cellular uptake assay by flow cytometry and confocal laser scanning microscopy

For flow cytometry ananlysis, HeLa cells were seeded in the 6-well plates (2×10^5 cells in 1 mL of DMEM per disk) and incubated for 24 h. Then Dox@AFBS with Dox concentration of 10 µg mL^{-1} was added to the wells. After incubation for 1 h, 2 h and 4 h at 37 °C, the cells were washed with PBS and detached with trypsin. Finally, the cells were resuspended in 400 µL of PBS for flow cytometric analysis on the BD FACSVerse™. For confocal laser scanning microscopy observation, HeLa cells were seeded in the culture disk (10^5 cells in 1 mL of DMEM per disk) and allowed to adhere overnight. Then Dox@AFBS were added to the disk. After incubation for 4 h and 12 h, the cells were washed with PBS and labeled with LysoTracker Green and stained with DAPI for confocal laser scanning microscopy (FV 1000, Olympus) imaging.

In vitro cytotoxicity assay

HeLa and HUVE cells were seeded in 96-well plates in sextuplicate (10^4 cells in 100 µL of DMEM per well) and allowed to adhere overnight. Then the medium was replaced with fresh culture medium containing AFBS with different bismuth concentrations. After incubation for 24 h, the standard CCK-8 assay was used to evaluate the cell viabilities relative to the control group. For in vitro RT analysis, HeLa cells incubated with AFBS at various bismuth concentrations were radiated under clinical 220 keV X-rays at a dose of 8 Gy, and the cell viability was evaluated by the CCK-8 assay. For chemotherapy analysis, HeLa cells were incubated with Dox@AFBS, Dox@AFn and Dox, respectively, for 24 h, and the cell viability was evaluated by the CCK-8 assay. For combinational treatment analysis, cells incubated with Dox@AFBS were subjected to RT treatment, and the cell viability was evaluated by the CCK-8 assay.

Xenograft tumor model

All animal experiments operations were in accord with the statutory requirements of People's Republic of China and care regulations approved by the administrative committee of laboratory animals of Shanghai Jiao Tong University. The xenograft HeLa tumor models were established by subcutaneous injection of 6×10^6 HeLa cells in 100 µL PBS into each mouse. When the tumor volume is above 75 mm^3, different treatments were carried out.

CT imaging

For in vitro CT imaging of Dox@AFBS at different bismuth concentrations, CT signal intensities in the region of interest were measured using a CT imaging system (SOMATOM Definition Flash, SIEMENS, Germany) with 80 kV, 50 mA and a slice thickness of 0.6 mm. For in vivo CT imaging, Dox@AFBS with a bismuth dose of 30 mg kg^{-1} and Dox dose of 3.75 mg kg^{-1}, was i.v. injected into HeLa tumor-bearing mice, and in vivo CT images were acquired pre-injection and at 24 h post-injection.

Biodistribution

The HeLa tumor-bearing mice after receiving administration of Dox@AFBS (bismuth dose of 30 mg kg^{-1} and Dox dose of 3.75 mg kg^{-1}) were sacrificed at the indicated time points (4 h, 1 d, 2 d, 6 d, 9 d and 12 d), and the bismuth contents in the main organs were analyzed using ICP-OES.

In vivo tumor therapy

HeLa tumor-bearing mice were randomly divided into eight groups (n = 5): i.e., control, Dox, Dox@AFn, AFBS, RT, AFBS+RT, Dox+RT, and Dox@AFBS+RT groups. The clinical 220 keV X-ray at a dose of 8 Gy was used for RT treatment, and the X-ray radiation area was fixed at 10 mm×10 mm. The bismuth dose is 30 mg kg^{-1} and Dox dose is 3.75 mg kg^{-1}. After various treatments, the weights of mice, and the lengths and widths of the tumors were recorded every 3 days for 12 days. The tumor volume was calculated according to the following formula: volume = width^2 × length/2. After various treatments for 3 days, tumors from different groups were dissected for H&E staining. After treatment for 12 days, H&E-stained major tissues from mice in Dox@AFBS+RT group were analyzed.

Statistical analysis

Quantitative data are expressed as mean ± standard deviation. Statistical comparisons were conducted by using one-way analysis of variance. Statistical significance was established at a value of $p < 0.05$.

Abbreviations

Dox: doxorubicin; RT: Radiotherapy; EPR: enhanced permeability and retention; CT: computed tomography; AFn: apoferritin; Dox@AFn: Dox-loaded AFn; Dox@AFBS: Bi$_2$S$_3$ nanocrystals synthesized on the Dox@AFn; TEM: transmission electron microscopy; AFBS: Bi$_2$S$_3$ nanocrystals synthesized with AFn; FTIR: fourier transform infrared spectroscopy; CD: circular dichroism; PBS: phosphate-buffered saline; FBS: fetal bovine serum; DMEM: Dulbecco's modified Eagle medium; DAPI: 4',6-diamidino-2-phenylindole; CCK-8: cell counting kit-8; ICP-OES: inductively coupled plasma optical emission spectrometry; HU: Hounsfield unit; i.v.: intravenously; H&E: hematoxylin and eosin.

Supplementary Material

Supplementary figures and table.
http://www.thno.org/v09p2779s1.pdf

Competing Interests

The authors have declared that no competing interest exists.

References

1. Mizutani H, Tada-Oikawa S, Hiraku Y, Kojima M, Kawanishi S. Mechanism of apoptosis induced by doxorubicin through the generation of hydrogen peroxide. Life Sci. 2005; 76: 1439-53.
2. O'Brien MER, Wigler N, Inbar M, Rosso R, Grischke E, Santoro A, et al. Reduced cardiotoxicity and comparable efficacy in a phase III trial of pegylated liposomal doxorubicin HCl (CAELYX (TM)/Doxil (R)) versus conventional doxorubicin for first-line treatment of metastatic breast cancer. Ann Oncol. 2004; 15: 440-9.
3. Pan LM, Liu JN, He QJ, Shi JL. MSN-Mediated Sequential Vascular-to-Cell Nuclear-Targeted Drug Delivery for Efficient Tumor Regression. Adv Mater. 2014; 26: 6742-8.
4. Liang MM, Fan KL, Zhou M, Duan DM, Zheng JY, Yang DL, et al. H-ferritin-nanocaged doxorubicin nanoparticles specifically target and kill tumors with a single-dose injection. Proc Natl Acad Sci U S A. 2014; 111: 14900-5.
5. Yu LD, Chen Y, Wu MY, Cai XJ, Yao HL, Zhang LL, et al. "Manganese Extraction" Strategy Enables Tumor-Sensitive Biodegradability and Theranostics of Nanoparticles. J Am Chem Soc. 2016; 138: 9881-94.
6. Peng LQ, Mei X, He J, Xu JK, Zhang WK, Liang RZ, et al. Monolayer Nanosheets with an Extremely High Drug Loading toward Controlled Delivery and Cancer Theranostics. Adv Mater. 2018; 30: 1707389.
7. Chen Q, Wang X, Wang C, Feng LZ, Li YG, Liu Z. Drug-Induced Self-Assembly of Modified Albumins as Nano-theranostics for Tumor-Targeted Combination Therapy. ACS Nano. 2015; 9: 5223-33.
8. Flenniken ML, Liepold LO, Crowley BE, Willits DA, Young MJ, Douglas T. Selective attachment and release of a chemotherapeutic agent from the interior of a protein cage architecture. Chem Commun. 2005: 447-9.
9. Fan KL, Jia XH, Zhou M, Wang K, Conde J, He JY, et al. Ferritin Nanocarrier Traverses the Blood Brain Barrier and Kills Glioma. ACS Nano. 2018; 12: 4105-15.
10. Kilic MA, Ozlu E, Calis S. A Novel Protein-Based Anticancer Drug Encapsulating Nanosphere: Apoferritin-Doxorubicin Complex. J Biomed Nanotechnol. 2012; 8: 508-14.
11. Ahn B, Lee SG, Yoon HR, Lee JM, Oh HJ, Kim HM, et al. Four-fold Channel-Nicked Human Ferritin Nanocages for Active Drug Loading and pH-Responsive Drug Release. Angew Chem Int Ed Engl. 2018; 57: 2909-13.
12. Mauceri HJ, Hanna NN, Beckett MA, Gorski DH, Staba MJ, Stellato KA, et al. Combined effects of angiostatin and ionizing radiation in antitumour therapy. Nature. 1998; 394: 287-91.
13. Begg AC, Stewart FA, Vens C. Strategies to improve radiotherapy with targeted drugs. Nat Rev Cancer. 2011; 11: 239-53.
14. Zhang XD, Luo Z, Chen J, Shen X, Song S, Sun Y, et al. Ultrasmall Au(10-12)(SG)(10-12) nanomolecules for high tumor specificity and cancer radiotherapy. Adv Mater. 2014; 26: 4565-8.
15. Her S, Jaffray DA, Allen C. Gold nanoparticles for applications in cancer radiotherapy: Mechanisms and recent advancements. Adv Drug Deliv Rev. 2017; 109: 84-101.
16. Al Zaki A, Joh D, Cheng ZL, De Barros ALB, Kao G, Dorsey J, et al. Gold-Loaded Polymeric Micelles for Computed Tomography-Guided Radiation Therapy Treatment and Radiosensitization. ACS Nano. 2014; 8: 104-12.
17. Wen L, Chen L, Zheng S, Zeng J, Duan G, Wang Y, et al. Ultrasmall Biocompatible WO$_{3-x}$ Nanodots for Multi-Modality Imaging and Combined Therapy of Cancers. Adv Mater. 2016; 28: 5072-9.
18. Zhang QH, Chen JW, Ma M, Wang H, Chen HR. A Bioenvironment-Responsive Versatile Nanoplatform Enabling Rapid Clearance and Effective Tumor Homing for Oxygen-Enhanced Radiotherapy. Chem Mater. 2018; 30: 5412-21.
19. Wang SG, Li X, Chen Y, Cai XJ, Yao HL, Gao W, et al. A Facile One-Pot Synthesis of a Two-Dimensional MoS$_2$/Bi$_2$S$_3$ Composite Theranostic Nanosystem for Multi-Modality Tumor Imaging and Therapy. Adv Mater. 2015; 27: 2775-82.
20. Ma M, Huang Y, Chen HR, Jia XQ, Wang SG, Wang ZZ, et al. Bi$_2$S$_3$-embedded mesoporous silica nanoparticles for efficient drug delivery and interstitial radiotherapy sensitization. Biomaterials. 2015; 37: 447-55.
21. Du JF, Gu ZJ, Yan L, Yong Y, Yi X, Zhang X, et al. Poly(Vinylpyrrolidone)-and Selenocysteine-Modified Bi$_2$Se$_3$ Nanoparticles Enhance Radiotherapy Efficacy in Tumors and Promote Radioprotection in Normal Tissues. Adv Mater. 2017; 29: 1701268.
22. Wang Y, Wu YY, Liu YJ, Shen J, Lv L, Li LB, et al. BSA-Mediated Synthesis of Bismuth Sulfide Nanotheranostic Agents for Tumor Multimodal Imaging and Thermoradiotherapy. Adv Funct Mater. 2016; 26: 5335-44.
23. Song GS, Liang C, Yi X, Zhao Q, Cheng L, Yang K, et al. Perfluorocarbon-Loaded Hollow Bi$_2$Se$_3$ Nanoparticles for Timely Supply of Oxygen under Near-Infrared Light to Enhance the Radiotherapy of Cancer. Adv Mater. 2016; 28: 2716-23.
24. Zhang XD, Chen J, Min Y, Park GB, Shen X, Song SS, et al. Metabolizable Bi$_2$Se$_3$ Nanoplates: Biodistribution, Toxicity, and Uses for Cancer Radiation Therapy and Imaging. Adv Funct Mater. 2014; 24: 1718-29.
25. Matsumura Y, Maeda H. A New Concept for Macromolecular Therapeutics in Cancer-Chemotherapy - Mechanism of Tumoritropic Accumulation of Proteins and the Antitumor Agent Smancs. Cancer Res. 1986; 46: 6387-92.
26. Peer D, Karp JM, Hong S, FaroKHzad OC, Margalit R, Langer R. Nanocarriers as an emerging platform for cancer therapy. Nat Nanotechnol. 2007; 2: 751-60.
27. Davis ME, Chen Z, Shin DM. Nanoparticle therapeutics: an emerging treatment modality for cancer. Nat Rev Drug Discov. 2008; 7: 771-82.
28. Wang ZT, Huang P, Jacobson O, Wang Z, Liu YJ, Lin LS, et al. Biomineralization-Inspired Synthesis of Copper Sulfide-Ferritin Nanocages as Cancer Theranostics. ACS Nano. 2016; 10: 3453-60.
29. Yang T, Wang Y, Ke HT, Wang QL, Lv XY, Wu H, et al. Protein-Nanoreactor-Assisted Synthesis of Semiconductor Nanocrystals for Efficient Cancer Theranostics. Adv Mater. 2016; 28: 5923-30.
30. Yang T, Tang YA, Liu L, Lv XY, Wang QL, Ke HT, et al. Size-Dependent Ag$_2$S Nanodots for Second Near-Infrared Fluorescence/Photoacoustics Imaging and Simultaneous Photothermal Therapy. ACS Nano. 2017; 11: 1848-57.
31. Huang P, Bao L, Yang DP, Gao G, Lin J, Li ZM, et al. Protein-Directed Solution-Phase Green Synthesis of BSA-Conjugated MxSey (M = Ag, Cd, Pb, Cu) Nanomaterials. Chem-Asian J. 2011; 6: 1156-62.
32. Yang WT, Guo WS, Le WJ, Lv GX, Zhang FH, Shi L, et al. Albumin-Bioinspired Gd:CuS Nanotheranostic Agent for In Vivo Photoacoustic/Magnetic Resonance Imaging-Guided Tumor-Targeted Photothermal Therapy. ACS Nano. 2016; 10: 10245-57.
33. Arumugam J, Raj AD, Irudayaraj AA, Thambidurai M. Solvothermal synthesis of Bi$_2$S$_3$ nanoparticles and nanorods towards solar cell application. Mater Lett. 2018; 220: 28-31.
34. Yang L, Guo YM, Ma XM, Hu ZG, Zhu SF, Zhang XY, et al. Cooperativity between pepsin and crystallization of calcium carbonate in distilled water. J Inorg Biochem. 2003; 93: 197-203.
35. Wilhelm S, Tavares AJ, Dai Q, Ohta S, Audet J, Dvorak HF, et al. Analysis of nanoparticle delivery to tumours. Nat Rev Mater. 2016; 1.